Induced seismicity red-light thresholds for enhanced geothermal prospects in the Netherlands

Schultz, Ryan; Muntendam-Bos, Annemarie; Zhou, Wen; Beroza, Gregory C.; Ellsworth, William L.

DOI
10.1016/j.geothermics.2022.102580

Publication date
2022

Document Version
Final published version

Published in
Geothermics

Citation (APA)
Schultz, R., Muntendam-Bos, A., Zhou, W., Beroza, G. C., & Ellsworth, W. L. (2022). Induced seismicity red-light thresholds for enhanced geothermal prospects in the Netherlands. *Geothermics*, *106*, Article 102580. https://doi.org/10.1016/j.geothermics.2022.102580

Geothermics 106 (2022) 102580

Contents lists available at ScienceDirect

Geothermics

journal homepage: www.elsevier.com/locate/geothermics

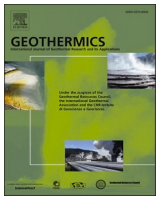

Induced seismicity red-light thresholds for enhanced geothermal prospects in the Netherlands

Ryan Schultz [a,*], Annemarie Muntendam-Bos [b,c], Wen Zhou [c], Gregory C. Beroza [a], William L. Ellsworth [a]

[a] Department of Geophysics, Stanford University, Stanford, CA, USA
[b] Central Expertise Department, Dutch State Supervision of Mines, The Hauge, the Netherlands
[c] Department of Geosciences and Engineering, Delft University of Technology, Delft, the Netherlands

ARTICLE INFO

Keywords:
Enhanced geothermal systems
Induced seismicity
Seismic hazard
Seismic risk
Traffic light protocols
Red-light

ABSTRACT

Prospects for geothermal energy in the Netherlands have renewed concerns around induced earthquakes. Risks from induced earthquakes are managed by traffic light protocols (TLPs), where the red-light is chosen as the stop-point before exceeding a tolerance to risk. Here, we simulate post-shut-in earthquake scenarios based on realistic information for the Netherlands. We focus on three risk metrics: aggregates like nuisance and damage impacts and also local personal risk (LPR) – a likelihood of building collapse fatality for an individual. Our results show that the severity of these risks varies spatially by orders of magnitude. Prior induced seismicity (e.g., the 2012 Huizinge event) provides a reference baseline to calibrate the Dutch earthquake risk tolerances. We find that these calibrated risk tolerances are similar to those observed in North America, suggesting an underlying sociological 'license to operate.' Furthermore, the use of calibrated risk tolerances results in nuisance concerns completely eclipsing the other two metrics. We compare our results to a hypothetical Groningen geothermal operation and find that our approach sets red-light thresholds approximately one magnitude unit below the M_L 3.6 Huizinge event. Overall, our results provide a first-order recommendation for red-light thresholds and proactive management of Dutch enhanced geothermal induced seismicity.

Plain language summary

The push to divest from fossil fuels has encouraged the development of geothermal energy in the Netherlands. Geothermal energy systems have the potential to induce earthquakes, which is significant because Groningen gas extraction induced earthquakes created public outrage that led to planned resource abandonment. Based on these concerns, we model the potential for induced earthquake risks (nuisance impacts, building damage, and chance of fatality). We also use the experience from the Groningen earthquakes to calibrate the Dutch tolerance to these risks. These risk metrics/tolerances are combined to determine when an enhanced geothermal system (EGS) should stop operations: i.e., the red-light threshold, reported as an earthquake magnitude. Our results suggest that the red-light threshold should change with location (M_L 1.8-3.0), primarily due to the distribution of population density. Nuisance is likely one of the most important risk metrics to consider because it consistently results in the lowest red-light magnitudes. A hypothetical EGS operation in Groningen would need a red-light threshold to be set one magnitude unit lower than the Huizinge event. Overall, our results provide a blueprint for the regulation of future earthquakes induced by geothermal stimulation.

1. Introduction

Concerns related to both climate change and energy security have driven an interest in developing greener energy sources (IEA, International Energy Agency, 2020). In the last decade, interest in the geothermal potential of the Netherlands has increased dramatically (van Heekeren and Bakema, 2015; Mijnlieff, 2020). The Dutch sedimentary rocks have been the primary focus of geothermal development, with regional characterization of reservoir properties estimating each 'play' likely hosts hundreds-of-thousands of PJ of heat in place [(Boxem et al., 2011); www.thermogis.nl]. Many of these plays target direct heat applications in hydrothermal, conductive, and low enthalpy/temperature regimes. Although, prospects have also expanded to consider deeper, hotter, and more impermeable reservoirs (UDG (Ultradiepe

* Corresponding author.
E-mail address: rjs10@stanford.edu (R. Schultz).

https://doi.org/10.1016/j.geothermics.2022.102580
Received 12 April 2022; Received in revised form 21 September 2022; Accepted 25 September 2022
Available online 28 September 2022

Geothermie) 2018). Particular to the Netherlands, the Lower Carboniferous Dinantian Carbonates (Fig. 1b) are an unproven but prospective play (Jaarsma et al., 2018; Veldkamp and Hegen, 2020). These carbonates have currently been targeted in the southeast of the Netherlands, where shallower (2.0-2.5 km depth) anticlinal carbonate structures are hosted within a basement-rooted horst block – structures that could provide fractures, faults, and karstification to aid permeability (Mijnlieff, 2020). In addition, the application of an enhanced geothermal system (EGS) (Olasolo et al., 2016) could further aid permeability by hydraulically stimulating fractures, particularly in areas where the play is located at greater depths.

These aforementioned considerations are aimed at optimizing geothermal production. However, prior experience with hydraulic fracturing of shale resources has shown that economically productive regions are often also earthquake susceptible regions (Pawley et al., 2018; Schultz et al., 2020b). That vertical proximity to basement-rooted faults (Schoenball and Ellsworth, 2017; Skoumal et al., 2018), lateral proximity to structurally controlled carbonates (Schultz et al., 2016), and hydrothermal fault-associated karstification (Galloway et al., 2018) aid hydraulic communication to critically stressed faults that induce earthquakes. EGS, the geothermal analogue to shale hydraulic fracturing, is also known to induce seismicity (Majer et al., 2007; Buijze et al., 2019; ter Heege et al., 2020) – with the largest such induced earthquake (M_W 5.5) occurring in Pohang, South Korea (Ellsworth et al., 2019). Impacts from the Pohang event were serious: resulting in a fatality, dozens of hospitalizations, 1700 people displaced, and 300+ million USD in economic damage. The Pohang earthquake resulted in the abandonment of this EGS project and spurred further calls to shutdown other injection/storage projects (Lee, 2019). In fact, geothermal related induced seismicity (up to M_L 1.7) has already been noted in the Netherlands (ter Heege et al., 2020; Muntendam-Bos et al., 2022).

These concerns around induced seismicity are compounded by the fact that the Netherlands has already had a contentious history of induced earthquakes (Dost and Haak, 2007; Muntendam-Bos et al., 2022). The most infamous case occurred within the Groningen province (Fig. 1a), where earthquakes were induced by the extraction of natural gas from Permian sandstones in the upper Rotliegend Group (van Thienen-Visser and Breunese, 2015; Vlek, 2019). Groningen earthquakes originally started in December 1991, gradually creating public tensions that peaked with the 2012 M_L 3.6 Huizinge event and subsequent analyses (Muntendam-Bos and De Waal, 2013; van der Voort and Vanclay, 2015). Despite significant research efforts (Bommer et al., 2017; Sintubin, 2018), public outrage eventually led to the decision to completely abandon the Groningen gas field, stranding ~800 billion m^3 of natural gas (Muntendam-Bos et al., 2022).

While these concerns are significant, they aren't insurmountable because tools to manage earthquake risks are available. Typically, induced earthquakes caused by shorter-term operations (e.g., fracture stimulation) are managed by traffic light protocol (TLPs) (Bommer et al., 2006; Baisch et al., 2019; Ader et al., 2020). TLP frameworks usually define the red-light threshold as the final stopping point before a regulatory intervention ceases operation completely (Bommer et al., 2015). Recent approaches have suggested translating seismic risks into equivalent red-light magnitude thresholds to better inform TLP designs (Schultz et al., 2020a, 2021b, 2021c). In this study, we adapt this risk-based approach to quantify the red-light threshold for potential earthquakes caused by EGS in the Netherlands. Similar to prior work, we find that risks vary spatially by orders of magnitude and that choosing a tolerance for risk allows for a fairer TLP design. In this case, we compare simulated risks from the 2012 Huizinge (M_L 3.6) event and the 1997 Roswinkel (M_L 3.4) event to calibrate the Dutch tolerance for risk. These results indicate that red-light thresholds should vary from M_L 1.8-3.0. We then discuss how these results fit into the context of TLP design and justify the importance of the risk metrics we considered.

2. Data and methods

The risk-based TLP approach can be broken into three broad categorical components: (1) a simulation of the earthquakes trailing the shut-in of an EGS operation, (2) computation of the anticipated ground

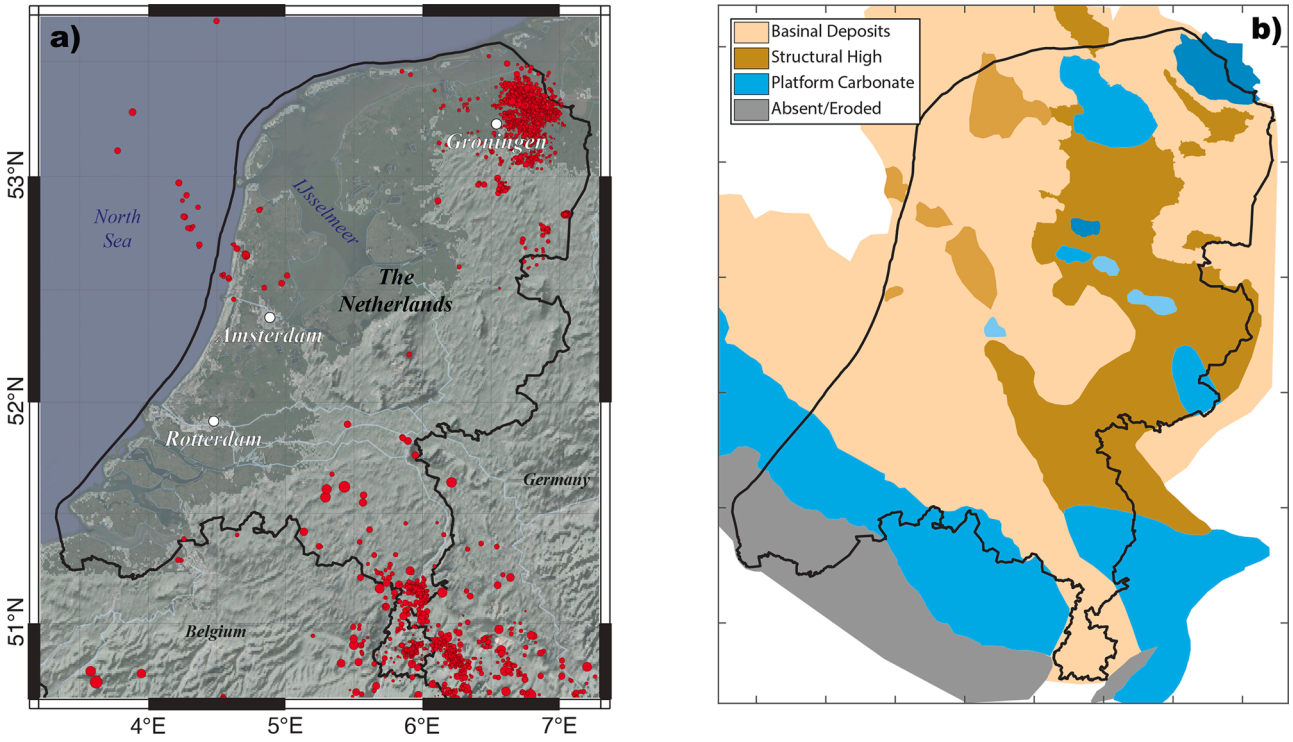

Fig. 1. Maps of the Netherlands, earthquakes, and Dinantian facies. a) Map of the Netherlands study area (black line), earthquakes (red circles) (KNMI 2022), and notable municipalities (white circles). b) Spatial distribution of Dinantian facies targeted for EGS, including Moliniacian-Livian and Warnantian substages (ten Veen et al., 2019).

shaking hazard for a given event, and (3) estimation of the exposure to seismic risks from the given hazard (Fig. 2). We combine these components in a Monte Carlo perturbation approach to build earthquake risk scenarios for all possible well locations in the Netherlands. Each of these components is elaborated on in the following subsections, and in prior work (Schultz et al., 2020a, 2021b, 2021c).

2.1. Trailing seismicity

The most important part to our analysis is the trailing seismicity model (Schultz et al., 2021b). Earthquake magnitudes following well shut-in are estimated using a concept similar to Båth's law for tectonic earthquake sequences, where the difference in magnitude between the mainshock and largest aftershock ΔM depends on the count ratio R_S, the b-value, and random variables u_i (Schultz et al., 2022).

$$\Delta M \approx \frac{1}{b} log_{10}\left(\frac{1}{R_S}\right) + \frac{1}{b} log_{10}\left(\frac{ln(u_1)}{ln(u_2)}\right) \quad (1)$$

In adapting this approach to EGS induced seismicity, we assume that a stimulation event larger than the red-light threshold occurs and prompts well shut-in. This event is then followed by additional aftershock-like events trailing shut-in. We inform our choice of b-value to be like those observed in the Netherlands and Groningen (Zöller and Holschneider, 2016; Dost et al., 2017; Muntendam-Bos and Grobbe, 2022): i.e., 0.95±0.09. The choice of count ratio is based on the beta distribution fit to empirical observation for hydraulic fracturing and EGS induced seismicity (Verdon and Bommer, 2020; Schultz et al., 2022). We justify this choice since it is based on a fit of all these operations, including regions with low tectonic seismic activity. As additional information becomes available for induced seismicity caused by EGS in the Netherlands, this distribution will be important to update. For further details on how induced earthquake magnitudes are simulated, we refer the reader to prior work (Schultz et al., 2020a, 2021b, 2021c, 2022).

In addition to simulating the trailing event magnitudes, we also simulate the depth distribution of EGS seismicity. The depth of the event is first guided by the 120°C isotherm (Figs. 3a and S1), a typical benchmark for economical geothermal electricity generation (Mijnlieff, 2020). Temperature-depth profiles are based on work characterizing the geothermal potential of the Netherlands (Békési et al., 2020, Veldkamp and Hegen, 2020). From this isotherm depth, the scenario earthquake depths are perturbed about a distribution that skews slightly in favour of deeper events (Fig. 4). This distribution is justified based on the observation that stimulation-induced events typically occur close to their stimulation interval, with some cases occurring on deeper basement-rooted faults (Schultz et al., 2020b).

2.2. Hazard calculation

The second component describes how these trailing earthquakes are translated into seismic hazard (Bommer, 2022). To do so, we use a ground motion prediction equation (GMPE) – a relationship that predicts the amount of earthquake ground shaking intensity as a function of magnitude, distance, depth, and site amplification (Bommer et al., 2021b). For the Netherlands, we use a GMPE recently developed for Groningen that estimates the peak ground velocity (PGV) (Bommer et al., 2021a). This GMPE has been found to be the best applicable for ground motion in the Netherlands (Ruigrok and Dost, 2020). To incorporate site amplification effects (Figs. 3b and S2), we also consider a global slope-based proxy for V_{S30} (Heath et al., 2020). Site amplification could also be updated with more sophisticated models, as they become available (van Ginkel et al., 2022). We consider variances in all of these models via their reported standard errors. We acknowledge that seismic radiation pattern will be an important parameter, but it is not included since earthquake focal mechanisms are usually unknown *a priori*.

While PGV is relevant for most of our risk metrics, we also need to consider a geometric average of the spectral acceleration periods (Eads et al., 2015) for building collapse, as it is sensitive to structural damage. Unfortunately, a suitably calibrated spectral acceleration GMPE does not exist for the Netherlands. We instead use a regionally calibrated relationship (Groningen dataset) to convert PGV into peak ground acceleration (PGA; Fig. S4), then convert PGA into spectral acceleration (Graizer and Kalkan, 2009), followed by a geometric averaging of the spectral acceleration periods. The range of periods averaged over (0.01s, 0.1s, 0.2s, 0.3s, 0.4s, 0.5s, 0.6s, 0.7s, 0.85s, and 1.0s) was chosen for consistency with fatality risk studies for Groningen (Crowley and Pinho, 2020). We test this model against the Groningen model, NGA West2, and the Atkinson induced seismicity GMPE [Boore et al., 2014; (Atkinson, 2015, Crowley and Pinho, 2020)] and find that spectral acceleration estimates are similar to NGA West2 which is typically predicts higher than the Groningen model (Fig. S5). While these conversions provide an adequate means to compute average spectral acceleration and are consistent with prior work (Bommer and Alarcon, 2006, Crowley and Pinho, 2020), more direct estimates of spectral acceleration would be preferred for future iterations.

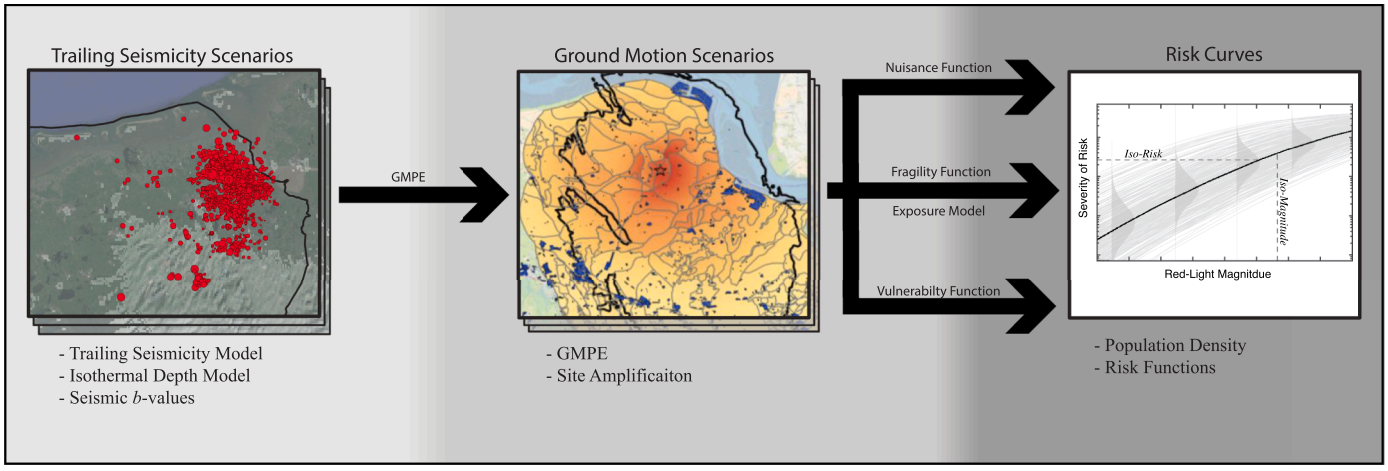

Fig. 2. The risk-based TLP approach. The workflow for determining red-light stopping thresholds from seismic risk is displayed schematically. Scenarios for the hypocentral parameters of the largest earthquake following EGS well shut-in are simulated (left panel), for each scenario ground shaking intensities are calculated spatially (middle panel), and the distribution of risks are determined as a function of red-light stopping magnitude (right panel). The Shake Map scenario is from a prior report (Spetzler and Evers, 2018).

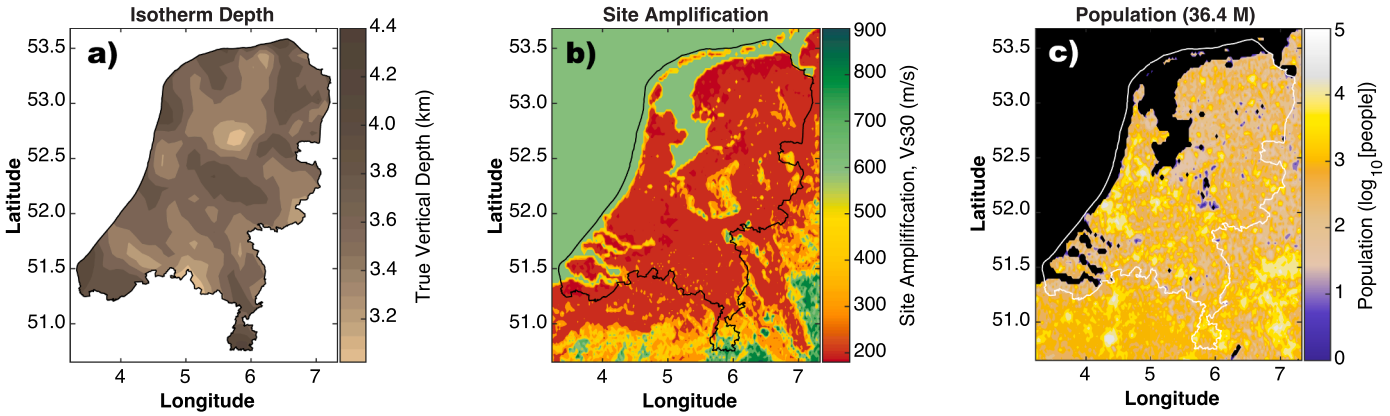

Fig. 3. Maps of the input parameters for the Netherlands. a) Depth contours for an isotherm of 120°C (Békési et al., 2020). b) Site amplification map, using slope-based V_{S30} as a proxy (Heath et al., 2020). c) Distribution of people throughout the Netherlands (Rose et al., 2019). See also Figs. S1, S2, and S3 for higher resolution versions.

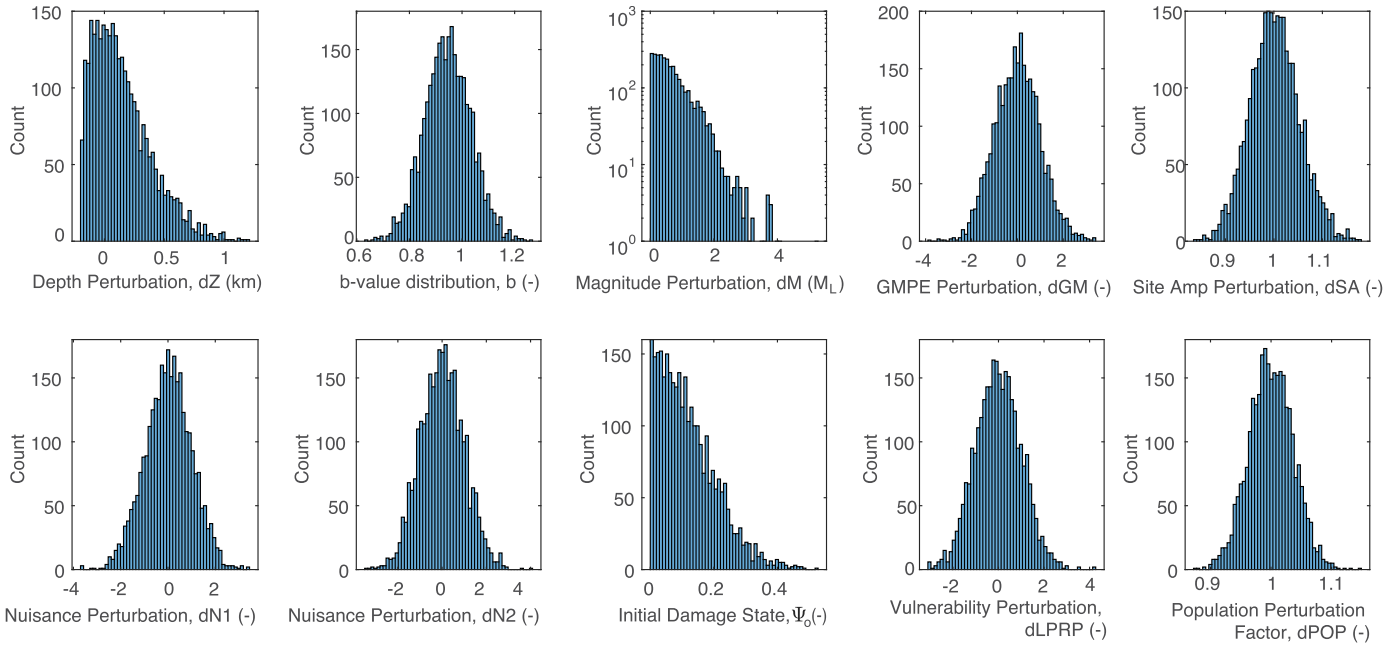

Fig. 4. Perturbed input variables for the Monte Carlo analysis. Ten panels show histograms for each of the perturbed variables of interest: dZ – depth, b – *b*-value, dM – trailing magnitude, dGM – GMPE variability, dSA – site amplification perturbation factor, dN1 and dN2 – nuisance function variabilities, Ψ_o – initial damage state, dLPR – vulnerability function variability, and dPOP – population perturbation factor.

2.3. Risk estimation

The third component describes a framework for translating earthquake hazards into seismic risks. In our approach, we are concerned with three distinct risk metrics: nuisance impacts, damage impacts, and chance of fatality. Nuisance/damage are aggregate risk metrics, measured by the number of households impacted. To begin estimating these metrics, we use nuisance/fragility functions to estimate the chance of nuisance/damage as a function of ground shaking intensity (Fig. S6). For the Netherlands, we use nuisance functions fitted to North American data (Schultz et al., 2021a) and fragility functions fitted to Groningen data (Korswagen et al., 2019). Both functions use PGV as their input ground shaking intensity. These functions further distinguish the degree of impact. For example, nuisance is distinguished by Community Decimal Intensity (CDI) (Wald et al., 2012) with the 2-6 levels roughly corresponding to the subjective criteria of just felt, exciting, somewhat frightening, frightening, and extremely frightening, respectively. Similarly, the Groningen fragility function is distinguished into damage states (DS) (Korswagen et al., 2019) with the 1-2 levels corresponding to criteria of visible light damage (>0.1 mm crack) and easily observable light damage (>1 mm crack), respectively. The third risk metric is an individual risk that considers a specific type of fatality chance: local personal risk (LPR), the likelihood that a fictional person inside of a building for 95% of their time will succumb to a building collapse death (SodM, Staatstoezicht op de Mijnen [State Supervision of Mines], 2014). We consider a predefined average-Groningen vulnerability function (Crowley and Pinho, 2020) that computes the chance of fatality as a function of period-averaged spectral acceleration. We justify this choice since the Groningen buildings can likely be considered as representative of most Dutch buildings. Our vulnerability and nuisance functions consider errors via a Gaussian representation of their logic tree branches and coefficient covariances, respectively (Fig. 4). Our damage functions also include a building pre-damage term Ψ_o (Korswagen et al., 2019), which we assign a half Gaussian distribution (0.00+0.15) for perturbations (Fig. 4).

In addition to computing these risk likelihoods, we require an

exposure model (Figs. 3c and S3). For this we use LandScan population distribution information (Rose et al., 2019) that provides a ~1×1 km grid of population information and assume an average of four residents per household. For aggregate risk metrics, we determine the total number of households impacted by summing the expected number of households impacted on each individual grid point. For computational convenience, we reduce this population grid to a resolution of 0.025×0.025°. Also, we do not simulate nuisance and damage impacts farther than 400 and 40 km, respectively–since impacts from moderate magnitude earthquakes beyond these distances are usually negligible (Nievas et al., 2020). To account for variability in population distributions, we perturb our population maps based on a Poisson-like distribution (i.e., a Gaussian with a standard deviation equal to the square root of the mean) for each grid point. For the individual risk metric of LPR, we only use this exposure model to ascertain the distance from the earthquake epicenter to the nearest populated grid point. When applicable, we also scale the population according to the temporal trends (Fig. S7) (Centraal Bureau voor de Statistiek 2021).

2.4. Monte Carlo sampling

The final point to consider is both a summary of individual components and a means to account for input variabilities. Each of the aforementioned components have significant variabilities that will influence the output risk metrics. To honour these variabilities, we use a 3000-trial Monte Carlo sampling approach in which all inputs are perturbed about their previously described distributions (Fig. 4). From these repeated trials, we build the statistical distribution of our risk metrics – where we will predominantly focus on the median values (Fig. 5). Thus, the resulting red-light thresholds represent the 50-50 chance of a given risk. For additional information on the workflow, we refer the reader to prior works on the subject (Schultz et al., 2020a, 2021b, 2021c).

3. Results

We are now able to apply this approach to potential EGS cases in the Netherlands (Fig. 5). We begin by assuming a single red-light threshold (i.e., iso-magnitude) to observe the spatial variations in our three metrics of risk, we then consider impacts from prior Groningen seismicity to constrain tolerances to these risks, and finally create iso-risk maps that determine red-light thresholds on these risk tolerances.

3.1. The iso-magnitude approach

First, we utilize our approach (Section 2) to determine the severity of risk for the geographic region of the Netherlands. To do so, we create an 'earthquake grid' of 0.100×0.100° on which we simulate potential EGS red-light earthquakes on. For each grid point, we assume a single red-light threshold of M_L 3.0. We choose this red-light threshold for two reasons: (1) this is 0.6 magnitude units below the 2012 Huizinge earthquake (+0.68 M is the mean ΔM value for our study's trailing seismicity inputs) and (2) this is the low end used for hydraulic fracturing TLPs in North America (Schultz et al., 2021c). That said, we acknowledge that this particular choice is somewhat arbitrary.

Based on this premise, our three risk metrics (nuisance, damage, and LPR) are spatially heterogeneous and vary by orders of magnitude (Fig. 6). The aggregate risk metrics (nuisance/damage impacts) show clear delineations that follow the spatial population distribution, differing by the length scale on which these changes take place. This difference in length scale has previously been explained by the typical range of damage/nuisance impacts for moderate magnitude earthquakes (i.e., 10s/100s of kms, respectively). On the other hand, LPR appears to spatially correlate most strongly with the isotherm depth (Figs. 3a and S1). This is because LPR is a local risk that we have estimated using the distance to the closest populated grid point. For the population distribution of the Netherlands (Fig. 3c), effectively this means that the epicentral distance is almost always 0 km, thus depth is effectively the only spatially varying input. This spatial variation in risk has previously been cited as a reason against iso-magnitude TLP designs (Schultz et al., 2021b, 2021c).

3.2. Calibration of risk tolerances

To be fairer in TLP design, an iso-risk approach could be followed instead. Complicating this, iso-risk approaches require that some value-based decision be made about the acceptable risk tolerances. Tolerances for risk will likely vary by region, depending on the reputational image of the operator and regulator (i.e., the social license to operate) (Richards, 2015). Here, we side-step these complications by examining prior induced earthquakes in the northeast Netherlands to measure these tolerances empirically. We consider all of the M3+ induced earthquakes in this region (Table 1) (KNMI 2022). In these scenarios, we bypass the trailing seismicity model and earthquake grid since we are

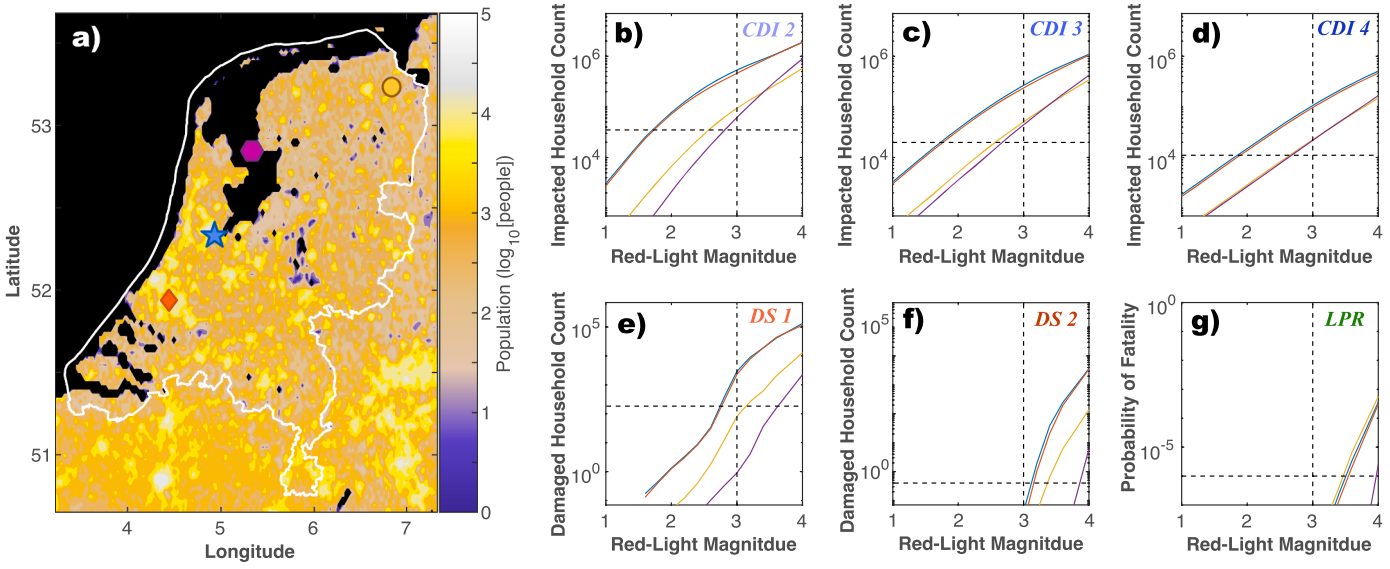

Fig. 5. Risk curves for four locations. a) Population map of the Netherlands showing the four locations sampled (coloured shapes). Median risk curves are plotted for nuisance at CDI 2 (b), CDI 3 (c), and CDI 4 (d) levels; damage levels of DS 1 (e) and DS 2 (f); and LPR (g). Median risk curves are colour coordinated with their map locations. Iso-risk (horizontal dashed line) and iso-magnitude (vertical dashed line) are shown for reference.

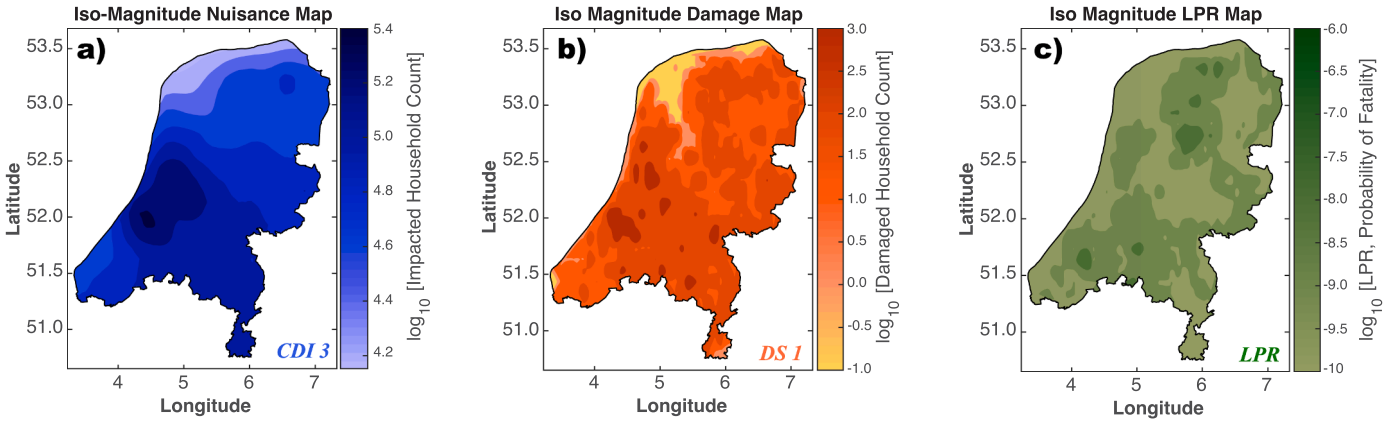

Fig. 6. Iso-magnitude risk maps. a) Number of households impacted by CDI 3 nuisance. b) Number of households impacted by DS 1 damage. c) Map of LPR, the probability of loss of life. All maps use a red-light threshold of M_L 3.0. All maps have their risk metrics colored on a base-10 logarithmic scale. Damage and LPR maps are truncated at 10^{-1} and 10^{-10}, respectively.

Table 1
Catalogue of all induced events (≥M_L 3.0) in the northeast Netherlands before and after the 2012 Huizinge event.

Name/Place	Date	Magnitude (M_L)	Latitude	Longitude	Depth (km)
Garrelsweer	2021-11-16	3.2	53.309	6.751	3.0
Westerwijtwerd	2019-05-22	3.4	53.328	6.652	3.0
Zeerijp	2018-01-08	3.4	53.363	6.751	3.0
Hellum	2015-09-30	3.1	53.234	6.834	3.0
't Zandt	2014-02-13	3.0	53.357	6.782	3.0
Garrelsweer	2013-07-02	3.0	53.294	6.785	3.0
Zandeweer	2013-02-07	3.2	53.389	6.667	3.0
Huizinge	2012-08-16	3.6	53.345	6.672	3.0
Garrelsweer	2011-06-27	3.2	53.303	6.787	3.0
Zeerijp	2009-05-08	3.0	53.354	6.762	3.0
Loppersum	2008-10-30	3.2	53.337	6.720	3.0
Westeremden	2006-08-08	3.5	53.350	6.697	3.0
Roswinkel	2000-10-25	3.2	52.832	7.052	2.3
Roswinkel	1998-07-14	3.3	52.833	7.053	2.0
Roswinkel	1997-02-19	3.4	52.832	7.038	2.0

considering impacts from past events with known magnitudes and locations. Instead of anticipating these parameters, we use the known catalogue details for these events (perturbed about their reported errors) (NORSAR 2018). As well, we fit the only free GMPE parameter (inter-event Z-score) based on observed shaking intensities (Dost and Haak, 1997; Dost and Kraaijpoel, 2013; Ruigrok and Dost, 2020; Ntinalexis et al., 2022). All further steps in our workflow proceed as normal with a 1000-trial Monte Carlo approach.

The estimation of the aggregate risk metrics is performed for all the earthquakes occurring before (Fig. S8) and after (Fig. S9) the 2012 Huizinge event. We find that the 2012 Huizinge event was likely the most impactful, by most of our risk metric estimates. We define most impactful as the largest mean of the 1000-trial Monte Carlo sample. The second most impactful events likely were the 1997 Roswinkel, 2006 Westeremden, and 2011 Garrelsweer events. For clarity, we focus our comparison between the 2012 M_L 3.6 Huizinge (Dost and Kraaijpoel, 2013) and the 1997 M_L 3.4 Roswinkel (Dost and Haak, 1997) events (Fig. 7) – where we consider the Huizinge event as the archetype of an intolerable amount of risk. For all three degrees of nuisance impacts (CDI 2-4), there is a clear separation (albeit with overlap) in the number of households that felt ground motion. For the damage impacts (DS 1-2), this separation is not clear; contrary to this, the Roswinkel event appears likely to have caused comparable amounts of damage to the Huizinge event. These comparable amounts of damage, despite differing ground motion, are likely due to the greater number of people at closer proximity to the Roswinkel epicentre (Fig. S10). We find separations of nuisance for the other larger/impactful events (Westeremdem and Garrelsweer) and mostly separated damage distributions (Figs. S8 and S9).

From these observations, we begin to infer risk tolerances. For nuisance tolerances, we consider the intersection between the Huizinge-Roswinkel nuisance impacts as an empirical measure of nuisance tolerance distribution. For damage tolerances, we consider the composite of the Huizinge-Roswinkel damage impacts as an empirical measure of damage tolerance distribution. From these empirical tolerance distributions, we select the 10^{th} percentile as our first choice for nuisance/damage tolerances. This 10^{th} percentile choice results in nuisance tolerances roughly similar to the modal value of the events smaller than Huizinge (Figs. 7, S8, and S9). We note that these tolerance estimates are not meaningfully changed if either the 2006 Westeremden or 2011 Garrelsweer events were considered instead of the 1997 Roswinkel event.

3.3. The iso-risk approach

Equipped with empirical tolerances for the aggregate risks, we apply the iso-risk approach to the Netherlands data. For tolerances to LPR, we use a probability of 10^{-6}, which is a low-end value typically used for this risk metric (Commissie-Meijdam 2015; Marzocchi et al., 2015). From this, we use the previously determined risk curves (Section 3.1) and the tolerances to risk (Section 3.2) to select spatially varying red-light thresholds.

Prior work on nuisance has focused on the CDI 3 degree of nuisance, partly due to unknown tolerances to this risk metric (Schultz et al., 2021b, 2021c). In the case of Groningen, we have empirically measured tolerances and may use all of them (Figs. 7, S8, and S9). Based on this line of reasoning, we build iso-nuisance maps for each of the CDI 2-4 degrees (Fig. 8a-8c). We incorporate each of these individual maps into an iso-nuisance combination map (Fig. 8d), by simply selecting the smallest red-light threshold among the three individual maps at each

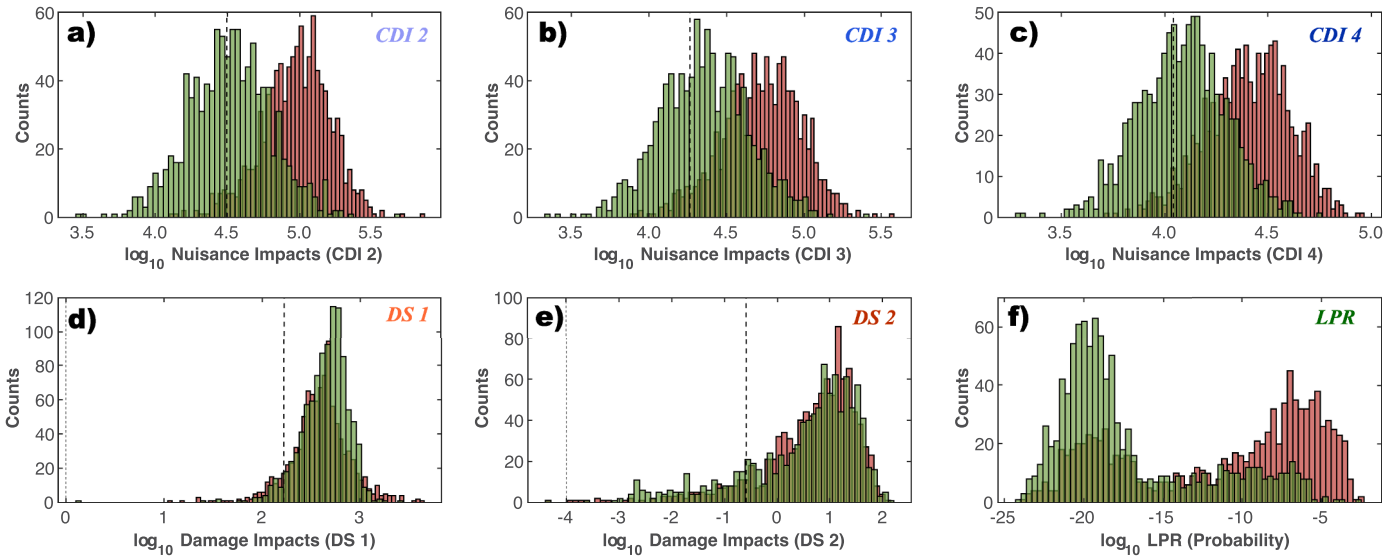

Fig.7. Earthquake impact scenarios. Comparison of risk metrics between the Roswinkel 1997-02-19 event (green bars) and the Huizinge 2012-08-16 event (red bars) alongside 10th percentile estimated tolerances for risk (dashed lines) and secondary tolerance choices (dotted lines). Risk metrics of nuisance (a-c), damage (d-e), and LPR (f) are considered.

grid point. With this combination approach, CDI 2 typically controls the thresholds in urban regions, CDI 3 in rural regions, and CDI 4 in remote regions (Fig. 8e). The differences in these individual iso-nuisance maps are subtle, varying by no more than +0.3 M_L from the combination map (Fig. S11). We note that the iso-nuisance combination map has an analogous spatial dependence on population distribution as the corresponding iso-magnitude map (Fig. 6a).

We apply the same logic to the damage impacts risk metric (Figs. S12 and S13); however, we find that doing so results in the nuisance metrics completely controlling the red-light combination map (Fig. S14). Instead, for interest's sake, we use even more risk-averse tolerances for damage risks (T_{DS1}=1; T_{DS2}=10^{-4}), where the ratio of damage tolerances (T_{DS1}/T_{DS2}) are kept relatively similar. We note that these new risk-averse choices are both well below the Huizinge-Roswinkel estimated tolerances (Fig. 7) and below the levels of damage expected for many of the M3+ events (Figs. 7, S8 and S9). We later provide some justification and discussion around this change of damage tolerance (Section 4.1). With these new damage risk tolerances, we next produce individual iso-damage maps that are then incorporated into an iso-damage combination map (Figs. S15 and S16). With this combination approach, DS 1 entirely controls the red-light thresholds. We note that the iso-damage combination map has an analogous spatial dependence on population distribution to the corresponding iso-magnitude map (Fig. 6b).

Third, an iso-LPR map is produced using the same logic as the previous risk metrics (Fig. 9c). We then produce a combined TLP that does not exceed any of our tolerances to risk by again choosing the smallest red-light threshold at each grid point (Fig. 10a). The median/mean values of this iso-risk combination map are ~M_L 2.4, ranging between M_L 1.8-3.0, with 10th/90th percentiles at roughly M_L 2.0/2.7, respectively (Fig. 11). When producing these combination maps, nuisance is the completely dominating concern followed by damage and then LPR. Damage-related thresholds only become relevant when the more risk-averse *ad hoc* damage tolerances are considered – even then, nuisance is still the controlling metric in most locations (Fig. 10b).

4. Discussion

We further discuss the implications these results have for effective TLP design.

4.1. Justification of risk metrics and risk tolerance choices

The first point we consider discussing is the justification of the risk metrics considered (and their tolerances) in our study. LPR is one of the more obvious choices, due to the general importance of keeping residents safe from bodily harm, the consideration of fatality in seismic risks from natural earthquakes (Marzocchi et al., 2015), the committee recommendations on the Groningen earthquakes (Commissie-Meijdam 2015), and the Dutch law (Ministry of Economic Affairs and Climate, 2022). Consideration of this risk metric is especially important since fatalities have already occurred from both EGS and hydraulic fracturing induced seismicity (Lei et al., 2019; Ellsworth et al., 2019). Many organizations define 'safe' tolerances to annual risks of death between 10^{-6} and 10^{-4}, depending on the source and consent to risk (Marzocchi et al., 2015). Similarly, the Groningen committee had recommended an annual tolerance of 10^{-5} (and a temporary 10^{-4} tolerance for buildings needing retrofitting) for gas extraction induced seismicity (Commissie-Meijdam 2015). This risk tolerance choice is comparable to anticipated requirements for EGS in the Dutch laws (Ministry of Economic Affairs and Climate, 2021).

When considering nuisance impacts, its incorporation as a seismic risk metric has yet to be established. Most jurisdictions have legal precedents that allow for the quiet enjoyment of their properties, including the Netherlands. The Groningen earthquakes have measurably impacted this enjoyment (Boelhouwer and van der Heijden, 2018). From this, it is reasonable to limit the exposure to unwanted ground shaking motions. In fact, some studies have also suggested the use of nuisance in TLP designs, with discussions around utilizing construction vibration guidelines (Cremen and Werner, 2020). Specific to determining the Dutch tolerances to nuisance impacts, the analysis on the prior Huizinge-Roswinkel events provides fairly strong evidence (Figs. 7, S8, and S9) – where the 2012 M_L 3.6 Huizinge event was likely the most impactful gas-extraction induced event in the Netherlands, from the perspective of nuisance. In this sense, the Huizinge earthquake is considered as an event that triggered social perception (and policy) changes (van der Voort and Vanclay, 2015; Schmidt et al., 2018) and is contrasted against the larger induced events that did not trigger a change (Roswinkel *et al*; Figs. 7, S8, and S9). We argue that our nuisance risk tolerance is appropriate (and important), as it is tied to a nuisance level that could trigger social unrest that spurs the complete abandonment of an EGS operation. Thus, linking a red-light threshold to a

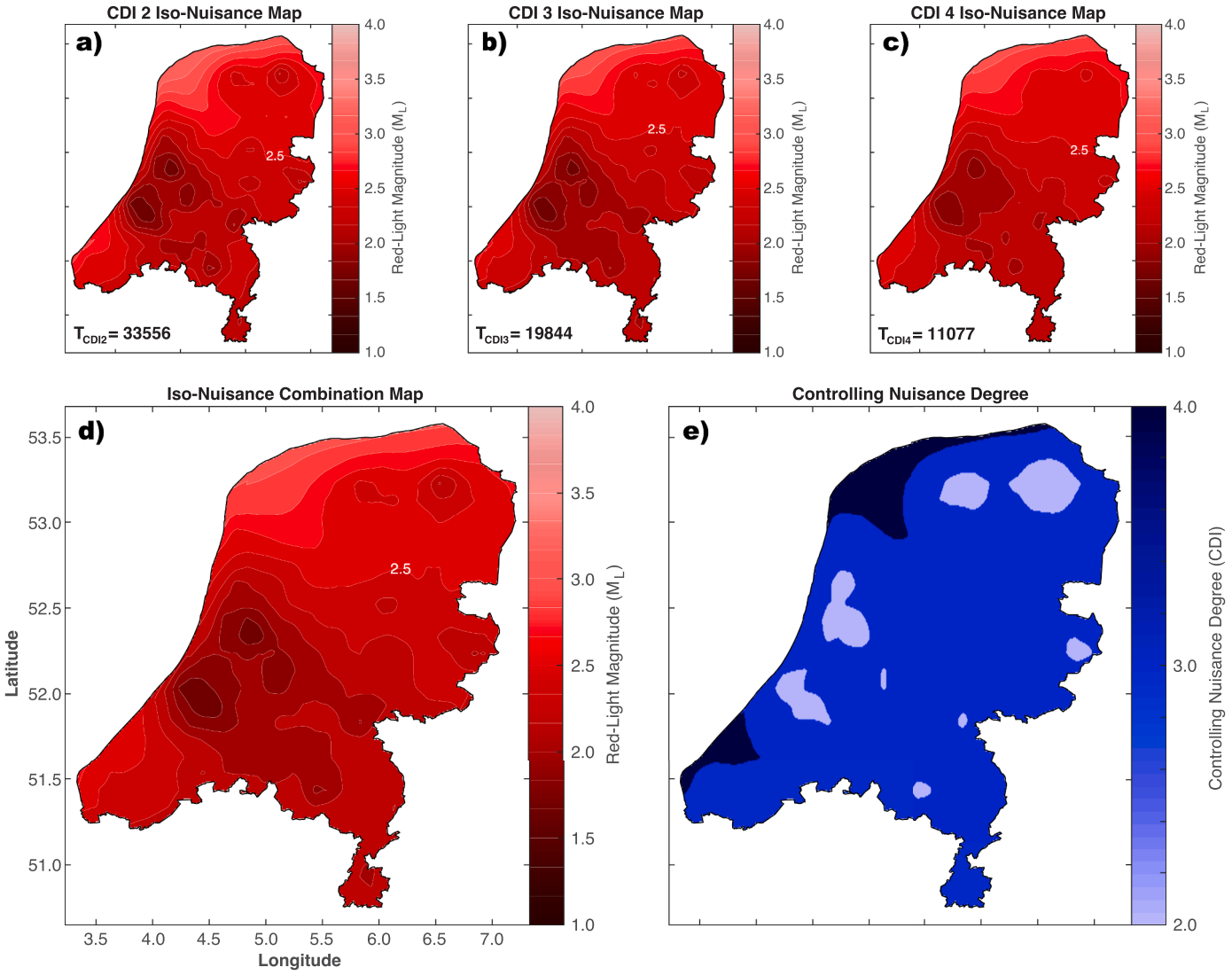

Fig. 8. Iso-nuisance and combination maps. Iso-nuisance maps are plotted for estimated tolerances at CDI 2 (a), CDI 3 (b), and CDI 4 (c). d) These three iso-nuisance maps are combined by taking the minimum red-light value at each grid point. e) Map showing which of the three iso-nuisance maps was the minimum red-light value for each grid point.

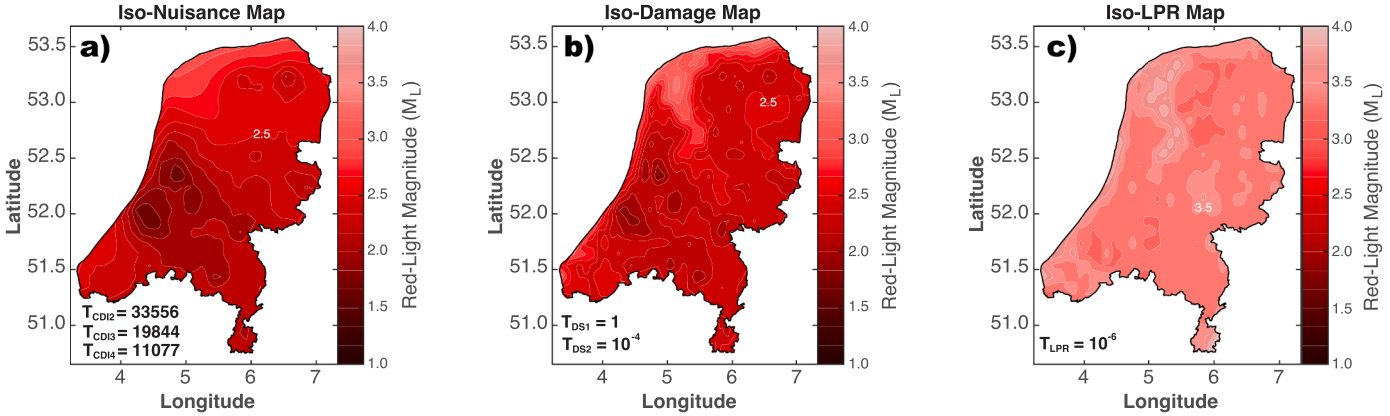

Fig. 9. Iso-risk maps. a) Combination map of the three iso-nuisance maps (Fig. 8d). b) Combination map of the two iso-damage maps (Fig. S15c). c) Iso-LPR map. All maps have their tolerances for risk displayed as text.

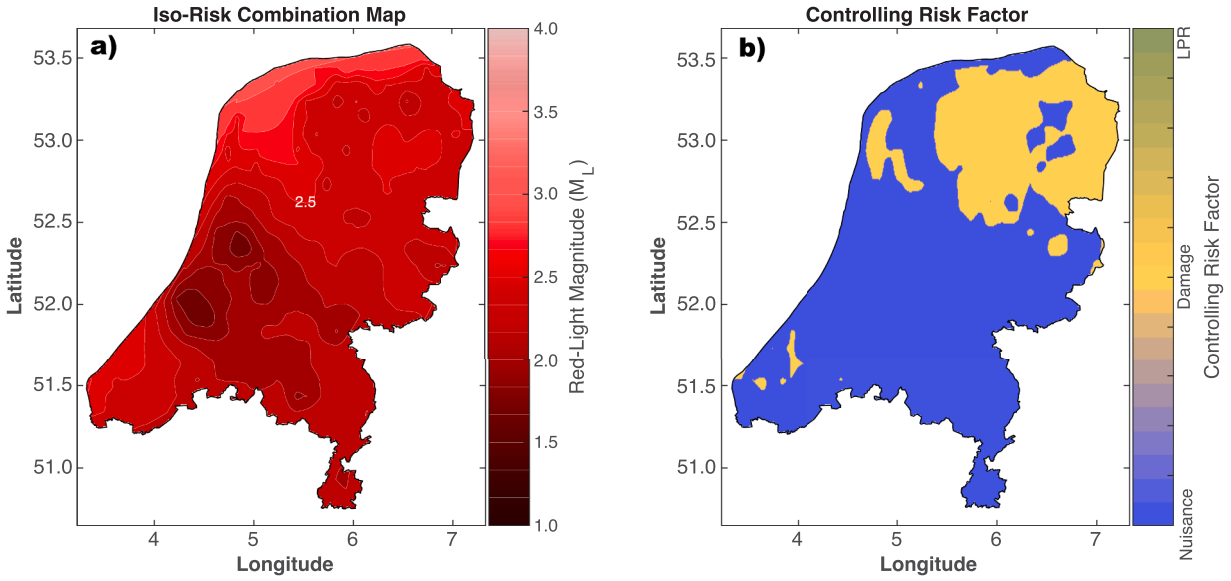

Fig. 10. Combination map. a) Combination map of the three iso-risk maps (Fig. 9). These three iso-risk maps are combined by taking the minimum red-light value at each grid point. b) Map showing which of the three iso-risk maps was the minimum red-light value for each grid point.

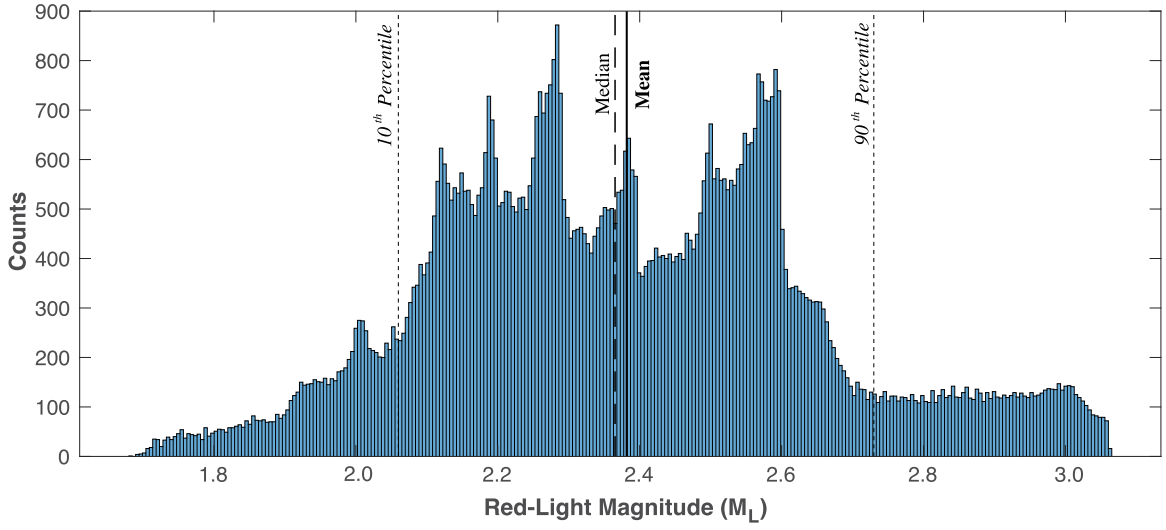

Fig. 11. Histogram of combination map red-light magnitudes. Red-light magnitudes for the footprint of the Netherlands (Fig. 10a) shown as a histogram (blue bars) alongside the 10^{th}/90^{th} percentiles (dotted lines), median (dashed line), and the mean (solid line).

nuisance level that risks losing the EGS operation is a suitable choice – since red-lights are defined as the last possible stopping point before a regulatory intervention is required. We further compare the Dutch estimates of nuisance tolerance (Fig. 12) to those previously described for North American hydraulic fracturing TLPs empirically (Schultz et al., 2021c). The tolerance for nuisance between the Netherlands and North America is surprisingly consistent, given the sharp distinction between federal resource-profit structure and provincial risk burden (van der Voort and Vanclay, 2015). This consistency suggests that nuisance tolerances may be a universally held threshold for the social license to operate (Richards, 2015).

Damage impacts are an important metric to consider in the sense that they are most directly tied to economic consequences, both direct and indirect. Generally speaking, many cases of induced seismicity are well known to have caused significant economic losses from building damage (Lei et al., 2019, Ellsworth et al., 2019). The Groningen province is particularly susceptible to damage because of earthquake prone building design, high site amplification (Figs. 3b and S2), and potential building damage from water-table adjustment in response to gas-extraction subsidence (Kooi et al., 2021) or natural peat/clay-related subsidence (van Asselen et al., 2018). Unfortunately, the analysis of the Huizinge-Rosswinkel events (Fig. 7) provides only limited information regarding Dutch tolerance to damage, suggesting 10^{th} percentile tolerances of T_{DS1}=183. It could be argued that a clear damage tolerance delineation cannot be made here because a single earthquake did not change perceptions around earthquake damage; instead, concerns may have grown alongside the accumulation of damage over the recurring Groningen earthquakes (Sarhosis et al., 2019). In this sense, there may be some qualitative justification for using a damage tolerance of T_{DS1}=1 to limit the growth of any damage in the first place. However, more data would be needed to discern potential cumulative, time-dependent, or changing tolerances to induced seismicity – likely by examining additional cases of new TLP implementation or resource abandonment. We also note that the use of these more risk averse tolerances is also bolstered by the legal requirement of operators being liable for induced earthquake damages in the Netherlands and thereby having to pay the

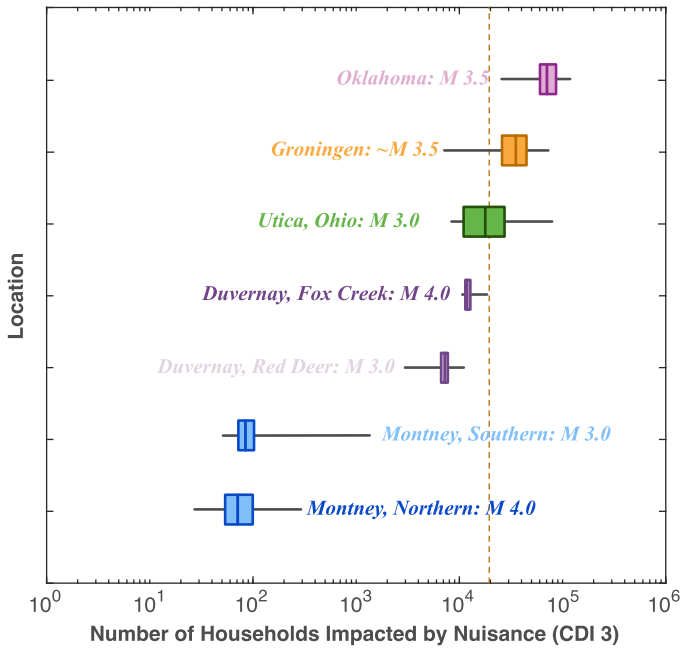

Fig. 12. Worldwide nuisance tolerance estimates. The distribution of CDI 3 nuisance tolerance (box-and-whisker plots; boxes show 25-50-75 percentiles) for Groningen (Fig. 7b) is compared to TLP estimates for hydraulic fracturing in North America (Schultz et al., 2021c). The 10^{th} percentile of the nuisance tolerance distribution, used to select the nuisance tolerance, is shown as an orange dashed line.

costs of repairs and retrofitting. It is worth pointing out that our model appears to underestimate the number of DS 1 damage reports by an order of magnitude [e.g., (den Bezemer and van Elk, 2018; van Elk and Doornhof, 2019)].

Overall, a combination of all these risk metrics will likely be important. Our approach has the advantage that multiple risk metrics (nuisance, damage, fatality) and types (local or aggregate) can be combined, by translating them into red-light thresholds. The three risk metrics considered here form a spectrum: from aggregate risks impacting many people, to individual risks that focus on the exposure of an individual. Nuisance impacts being at the most aggregate end of the spectrum, evidenced by their longer range of influence for moderate magnitude events (Figs. 6 and 9) and relatively large numbers of people impacted for their tolerance levels. Thus, iso-nuisance maps capture the larger trends, ensuring large numbers of people are not exposed to unwanted ground shaking; iso-damage maps ensure that rural towns (smaller than the nuisance tolerances) in remote regions are not exposed to unwanted damage that is glossed over by iso-nuisance; and iso-LPR maps work on the smallest scales to ensure that no individual is exposed to undue personal risk. An example of this is noted with the inclusion of multiple degrees of nuisance risks (Fig. 8), where differing densities of populations influence the controlling nuisance degree (i.e., CDI 2-4). This line of reasoning is particularly true for regions (like North America) that have large population disparities/concentrations (Schultz et al., 2021b, 2021c). However, for the Netherlands, much of the country's land is fairly densely populated with subtler transitions between urban and rural areas (Figs. 3c and S3). Because of this, nuisance impacts are typically the dominant concern (Figs. 10 and S14). Of course, these trends depend strongly on the jurisdiction's tolerance to each risk metric – the currently calibrated tolerances suggest that the Dutch are most sensitive to the nuisance risk metric.

Once red-lights thresholds have been defined, it is possible to tie the choice of yellow-light thresholds to the red-light (Schultz et al., 2020a). Yellow-lights are intended to provide operators with a window to enact mitigation strategies before reaching the red-light threshold. The possibility of magnitude 'jumps' (Verdon and Bommer, 2020) allows for straight from green-to-red scenarios to occur. Thus, the choice of the yellow-light threshold needs to be an appropriate magnitude gap from the red-light threshold to prevent this from occurring. Prior work (Schultz et al., 2020a) had suggested that using a yellow-light that is 2.0 magnitude units less than the red-light is usually adequate – depending on a jurisdiction's tolerance for risk.

4.2. A hypothetical EGS operation in Groningen

We also discuss how our results would apply to a hypothetical EGS operation that occurred in Groningen, to compare against the previous gas extraction induced events. Additionally, we compare how each risk metric contributes to the red-light threshold and further justify the use of multiple risk metrics. To do so, we examine our risk curves for the location of the 2012 Huizigne event, normalized on the tolerances to risk previously described (Fig. 13). For an EGS operation in this location, we note that the first red-light threshold is approximately M_L 2.5 for DS 1 and all of the nuisance CDI 2-4 are encompassed by M_L 2.7. The DS 2 threshold is next at M_L ~3.0, followed by the 10^{-6}-10^{-4} LPRs between M_L 3.5-3.9. Red-light thresholds based solely on LPR would anticipate nuisance impacts roughly an order of magnitude higher than the calibrated Dutch tolerances. This is significant since our calibrated nuisance tolerance has the potential to terminate an (EGS) operation due to social outrage.

We note that all the risk curves produce red-light thresholds that are lower than the M_L 3.6 of the Huizinge event. In particular, the nuisance red-light thresholds are approximately one magnitude unit smaller than M_L 3.6 – despite the Huizinge-Roswinkel events being used to calibrate the tolerance for nuisance (Fig. 7). This can dominantly be understood via the trailing seismicity model (Schultz et al., 2022), which anticipates a mean value of +0.68 ΔM for our study's input parameters. In this sense, the red-light threshold has been automatically stepped back from event magnitudes that would likely be consequential to account for trailing seismicity. Other smaller contributions come from perturbations to the remaining input features; likely the ground motion variability is dominant, similar to disaggregation of seismic risk in Groningen (van Elk et al., 2017). Overall, this hierarchy of perturbed value importance is comparable to sensitivity tests that found trailing seismicity to be the dominant risk factor to consider (Schultz et al., 2021b). Our results demonstrate that incorporating a consideration of trailing seismicity in red-light TLP design is necessary.

4.3. Equivalent risks from an LPR-based red-light threshold

To continue building on the arguments that each risk metric is important, we consider the case in which red-light thresholds were determined solely by the LPR metric. Guided by Dutch law, we first use a tolerance of 10^{-5} to determine the iso-LPR red-light thresholds. Then we use this iso-LPR red-light threshold to estimate the amount of risk anticipated for the Netherlands (Fig. 14). In this case, essentially all grid points have risk impacts greater than the Huizinge-Roswinkel calibrated tolerances. Nuisance risks are typically an order of magnitude larger than the calibrated tolerances for all of the levels considered (i.e., CDI 2-4). Damage tolerances are typically 1-2 orders of magnitude larger than the calibrated tolerances (T_{DS1}=183; T_{DS2}=0.4) for all of the levels considered (i.e., DS 1-2). This analysis demonstrates that a red-light threshold designed solely on LPR would allow impacts significantly greater than the 2012 Huizinge earthquake: an event that arguably led to the abandonment of the Groningen gas field. Instead, incorporating risk metrics like nuisance/damage allows for their consideration in TLP design alongside LPR (Fig. 10a).

4.4. Limitations of our model and results

Here we discuss some of the limitations of our model and the derived

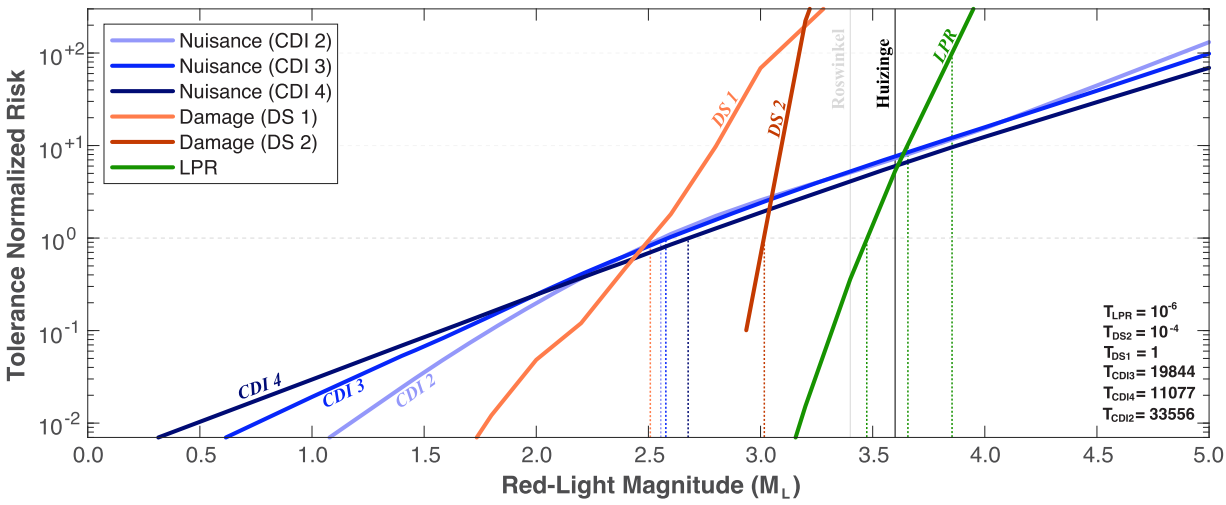

Fig. 13. Red-light thresholds for a hypothetical Huizinge EGS operation. Risk curves (solid lines) are shown for the Huizinge location (see legend). All risk curves are normalized by their tolerances (text inset), such that the 10° crossing is always the red-light threshold (vertical dotted lines). For context, corresponding red-light thresholds are compared against the magnitude of the Roswinkel 1997-02-19 and Huizinge 2012-08-16 events (vertical solid lines).

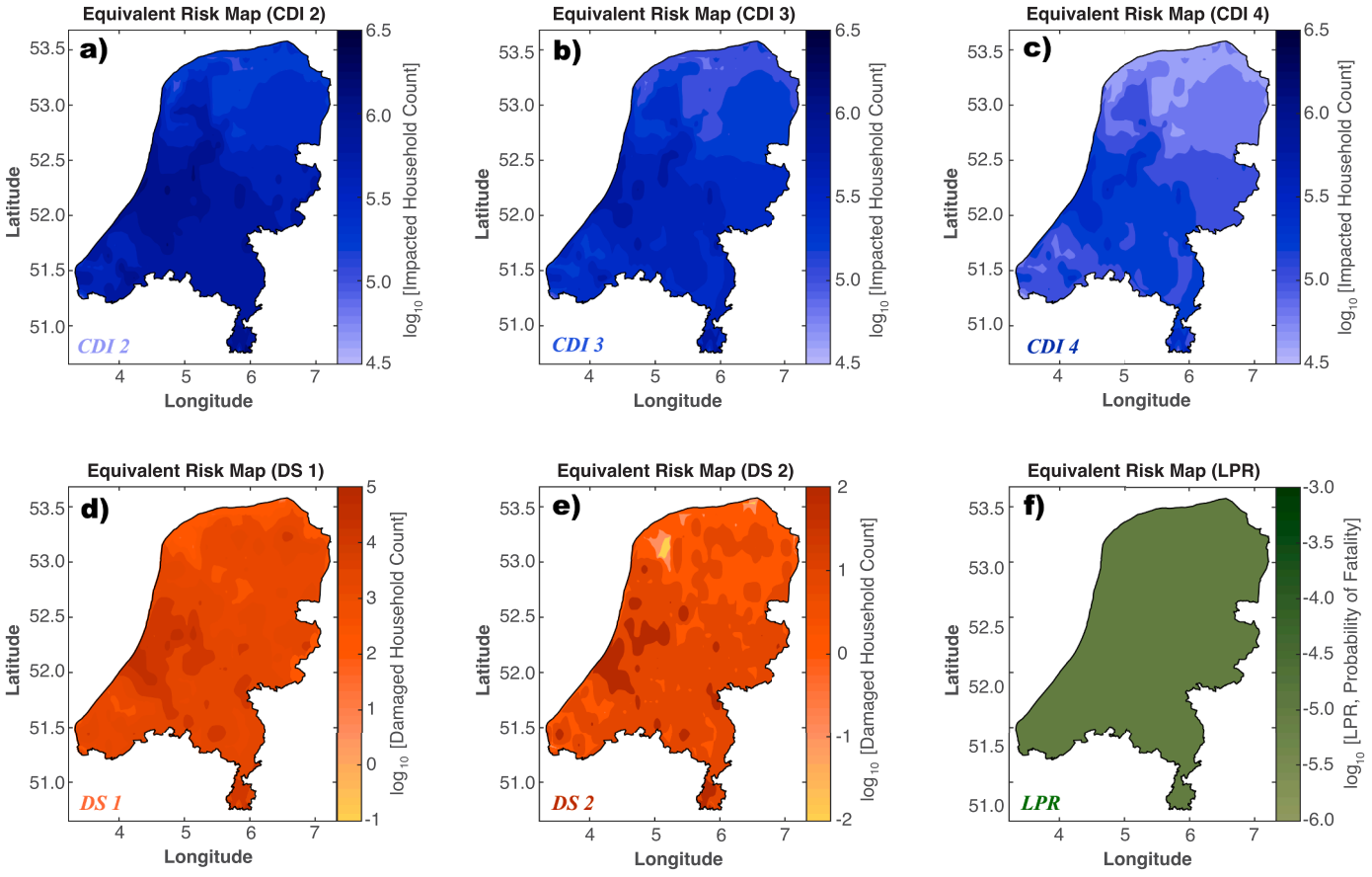

Fig. 14. Equivalent risk maps. If red-light thresholds were determined solely by iso-LRP at 10−5, these are the estimated amount of impact for each risk metric. Risk metrics of nuisance (a-c), damage (d-e), and LPR (f) are considered.

results. First, the results of this study are largely derived from a translation of the most relevant material (either natural or Groningen extraction-related seismicity) to an anticipated problem of EGS caused earthquakes. As EGS induced earthquakes begin to occur, these models will require refinement and updates – especially as the EGS earthquakes begin to challenge the current model assumptions. We note that our workflow is flexible in the sense that new models can be interchanged/updated. For example, during the review process of this paper, a new fragility function has been developed (Korswagen et al., 2022) that could replace our current fragility (Korswagen et al., 2019). If potential EGS induced earthquakes in the Netherlands were found to be restricted to a smaller geographic region, more targeted risk approaches that use known building inventories could be applied. Additionally, future applications of this approach would benefit from the use of wavefield

correlation in deriving spatial estimates of ground motion (Stafford et al., 2019). Specifically, this could be introduced as an additional parameter to sample on during Monte Carlo analysis, to better account for spatial biases in the locations of felt, damaging, or harmful ground shaking.

In our analysis we have focused on median values of the risk curves. Median values have the statistical interpretation of being the 50-50 chance of a given risk impact. However, mean values have the more informative statistical interpretation of being the expected amount of a risk impact. Hence the use of mean LPR values in induced seismicity laws for the Netherlands (Ministry of Economic Affairs and Climate 2021, 2022). Despite this, we have focused on the median due to current model limitations – particularly with the estimation of LPR. The heavy-tailed nature of our risk metrics suggests that the mean will be strongly influenced by small-likelihood, high-consequence events. Particularly important to better constraining these types of events will be a better understanding of maximum possible magnitudes to truncate the upper magnitude of trailing events, a regional calibration of shut-in count ratios, and better ground motion models in the Netherlands (that directly compute spectral acceleration and are validated for extrapolation to larger magnitudes). We note that for the skewness of all our risk metrics, the mean values are always larger than median. Thus, considering mean values instead of median would result in lower red-light thresholds.

We also briefly note that our analysis has been tailored to induced seismicity as a result of EGS stimulation. This because the trailing seismicity model (Schultz et al., 2022) has been calibrated on shorter-term stimulation induced events. The incorporation of longer-term seismicity induced by geothermal production would require either a general or locally calibrated trailing seismicity model that captures the effects of geothermal production induced earthquakes.

In addition to these considerations, one of the current impediments to our approach is the accurate calibration of risk tolerances. For many of the risk metrics the choice of tolerance can be ambiguous and vary over orders of magnitude: depending on familiarity with risk, consent to risk, and the risk type (Marzocchi et al., 2015). Compounding this, the selection of risk tolerances can substantially influence red-light thresholds (Schultz et al., 2021b). In this study, we have attempted to place more rigorous and empirical estimates to these tolerances (e.g., Sections 3.2 and 4.1). Directed research and policy developments could address some of these issues: for example, through future studies that quantified links between risk tolerance and the social license to operate via surveys (Cousse et al., 2021) and through strong policy that makes clear and well-informed recommendations on risk tolerances (Commissie--Meijdam 2015).

5. Conclusions

In summary, we have applied a risk-based approach to design a TLP that manages prospective EGS induced seismicity. We lean on the previously developed seismic hazard/risk research for Groningen gas field. We analyzed the 2012 M_L 3.6 Huizinge and 1997 M_L 3.4 Roswinkel events to calibrate tolerances to nuisance/damage risks. We found that nuisance impacts put more strict bounds on operations than damage impacts and LPR for the Netherlands. Moreover, the calibrated tolerances for nuisance risk are comparable to those determined for hydraulic fracturing in North America. The combination of these three risk metrics (nuisance impacts, damage impacts, and LPR) provides a quantitative basis for reference red-light thresholds to inform future EGS TLPs.

Author Contributions

R.S. and A.M. conceived the project. R.S. collected data, carried out the analysis, and wrote the manuscript with guidance, comments, and revisions from all the authors. A.M. and W.Z. supported in collecting data and performing analyses.

Declaration of Competing Interest

The authors declare the following financial interests/personal relationships which may be considered as potential competing interests

Acknowledgments

We would like to thank Estzer Békési, Julian Bommer, Helen Crowley, and David Wald for assistance in directing us to the appropriate data and models used in this study. We would like to thank two anonymous reviewers for their critiques that helped improve this manuscript. Funding for this work came from the Stanford Center for Induced and Triggered Seismicity and the DEEP project which has been subsidized through the Cofund GEOTHERMICA by DETEC (CH), DoE (USA), MEDDE (FR), Jülich (DE), DCCAE/GSI (IRL), and RVO (NL). Geothermal gradient (Békési et al., 2020), trailing seismicity model (Schultz et al., 2022), GMPE model (Bommer et al., 2021b), site amplification (Heath et al., 2020), population density (Rose et al., 2019), nuisance function (Schultz et al., 2021a), fragility function (Korswagen et al., 2019), vulnerability function (Crowley and Pinho, 2020), earthquake catalogue (KNMI 2022), and ground motion databases (Dost and Haak, 1997, Dost and Kraaijpoel, 2013, Ruigrok and Dost, 2020, Ntinalexis et al., 2022) are derived from prior studies. Routines and publicly available data used to create the figures and results of this paper can be found online at https://github.com/RyanJamesSchultz/riskTLPnl. Additional materials on the workflow are also discussed in prior studies (Schultz et al., 2021b, Schultz et al., 2021c).

Supplementary materials

Supplementary material associated with this article can be found, in the online version, at doi:10.1016/j.geothermics.2022.102580.

References

and Ader, T., Chendorain, M., Free, M., Saarno, T., Heikkinen, P., Malin, P.E., Vuorinen, T., 2020. Design and implementation of a traffic light system for deep geothermal well stimulation in Finland. J. Seismol. 24 (5), 991–1014. https://doi.org/10.1007/s10950-019-09853-y.

Atkinson, G.M., 2015. Ground-motion prediction equation for small-to-moderate events at short hypocentral distances, with application to induced-seismicity hazards. Bull. Seismol. Soc. Am. 105 (2A), 981–992. https://doi.org/10.1785/0120140142.

Baisch, S., Koch, C., Muntendam-Bos, A., 2019. Traffic light systems: to what extent can induced seismicity be controlled? Seismol. Res. Lett. 90 (3), 1145–1154. https://doi.org/10.1785/0220180337.

and Békési, E., Struijk, M., Bonté, D., Veldkamp, H., Limberger, J., Fokker, P.A., van Wees, J.D., 2020. An updated geothermal model of the Dutch subsurface based on inversion of temperature data. Geothermics 88, 101880. https://doi.org/10.1016/j.geothermics.2020.101880.

Boelhouwer, P., van der Heijden, H., 2018. The effect of earthquakes on the housing market and the quality of life in the province of Groningen, the Netherlands. J. Hous. Built Environ. 33 (2), 429–438. https://doi.org/10.1007/s10901-018-9600-y.

Bommer, J.J., Alarcon, J.E., 2006. The prediction and use of peak ground velocity. J. Earthq. Eng. 10 (01), 1–31.

and Bommer, J.J., Oates, S., Cepeda, J.M., Lindholm, C., Bird, J., Torres, R., Rivas, J., 2006. Control of hazard due to seismicity induced by a hot fractured rock geothermal project. Eng. Geol. 83 (4), 287–306. https://doi.org/10.1016/j.enggeo.2005.11.002.

Bommer, J.J., Crowley, H., Pinho, R., 2015. A risk-mitigation approach to the management of induced seismicity. J. Seismol. 19 (2), 623–646. https://doi.org/10.1007/s10950-015-9478-z.

... and Bommer, J.J., Stafford, P.J., Edwards, B., Dost, B., van Dedem, E., Rodriguez-Marek, A., Ntinalexis, M., 2017. Framework for a ground-motion model for induced seismic hazard and risk analysis in the Groningen gas field, the Netherlands. Earthq. Spectra 33 (2), 481–498. https://doi.org/10.1193/082916EQS138M.

Bommer, J.J., Stafford, P.J., Ntinalexis, M., 2021a. Empirical equations for the prediction of peak ground velocity due to induced earthquakes in the groningen gas field – October 2021. NAM Report 44.

Bommer, J., Edwards, B., Kruiver, P., Rodriguez-Marek, A., Stafford, P., Dost, B., Ntinalexis, M., Ruigrok, E., Spetzler, J., 2021b. V7 NAM Repo. 282. Ground-motion model for induced seismicity in the groningen gas field with assurance letter.

Bommer, J.J., 2022. Earthquake hazard and risk analysis for natural and induced seismicity: towards objective assessments in the face of uncertainty. Bull. Earthq. Eng. 20 (6), 2825–3069. https://doi.org/10.1007/s10518-022-01357-4.

... and Boxem, T.A.P., Van Wees, J.D., Pluymaekers, M.P.D., Beekman, F., Batini, F., Bruhn, D., Schellschmidt, R., 2011. ThermoGIS world aquifer viewer-an interactive geothermal aquifer resource assessment web-tool. In 1st EAGE Sustainable Earth Sciences (SES) conference and exhibition. European Association of Geoscientists and Engineers, pp. cp–268. https://doi.org/10.3997/2214-4609.20144176.

... and Buijze, L., van Bijsterveldt, L., Cremer, H., Paap, B., Veldkamp, H., Wassing, B.B., Jaarsma, B., 2019. Review of induced seismicity in geothermal systems worldwide and implications for geothermal systems in the Netherlands. Neth. J. Geosci. 98. https://doi.org/10.1017/njg.2019.6.

Centraal Bureau voor de Statistiek, 2021. Temporal population trends for Netherlands and Groningen. Opendata.cbs.nl.

Commissie-Meijdam, 2015. Eindadvies Handelingsperspectief voor Groningen Adviescommissie 'Omgaan met risico's van geïnduceerde aardbevingen' 37.

Cousse, J., Trutnevyte, E., Hahnel, U.J., 2021. Tell me how you feel about geothermal energy: affect as a revealing factor of the role of seismic risk on public acceptance. Energy Policy 158, 112547. https://doi.org/10.1016/j.enpol.2021.112547.

Crowley, H., Pinho, R., 2020. Report on the fragility and consequence models for the groningen field (Version 7). NAM Report 83.

den Bezemer, T., van Elk, J., 2018. Special Report on the Zeerijp Earthquake –8th January 2018. *NAM Report* 61.

Dost, B., Haak, H.W., 1997. Macroseismische waarnemingen Roswinkel *19-2-1997. KNMI Technisch Rapport TR-199*. Royal Netherlands Meteorological Institute (KNMI, p. 9.

(2007) Dost, B., Haak, H.W., 2007. Natural and induced seismicity. In: Wong, T.E., Batjes, D.A.J., De Jager, J. (Eds.), Geology of the Netherlands. Royal Netherlands Academy of Arts and Sciences (Amsterdam), pp. 223–239.

Dost, B., Kraaijpoel, D., 2013. The august 16, 2012 earthquake near Huizinge (Groningen). *KNMI Scientific Report. Royal Netherlands Meteorological Institute (KNMI)*, Utrecht, The Netherlands 26.

Dost, B., Ruigrok, E., Spetzler, J., 2017. Development of seismicity and probabilistic hazard assessment for the Groningen gas field. Neth. J. Geosci. 96 (5), s235–s245. https://doi.org/10.1017/njg.2017.20.

Eads, L., Miranda, E., Lignos, D.G., 2015. Average spectral acceleration as an intensity measure for collapse risk assessment. Earthquake Eng. Struct. Dyn. 44 (12), 2057–2073. https://doi.org/10.1002/eqe.2575.

Ellsworth, W.L., Giardini, D., Townend, J., Ge, S., Shimamoto, T., 2019. Triggering of the Pohang, Korea, earthquake (M w 5.5) by enhanced geothermal system stimulation. Seismol. Res. Lett. 90 (5), 1844–1858. https://doi.org/10.1785/0220190102.

Galloway, E., Hauck, T., Corlett, H., Pană, D., Schultz, R., 2018. Faults and associated karst collapse suggest conduits for fluid flow that influence hydraulic fracturing-induced seismicity. Proc. Natl. Acad. Sci. 115 (43), E10003–E10012. https://doi.org/10.1073/pnas.1807549115.

Graizer, V., Kalkan, E, 2009. Prediction of spectral acceleration response ordinates based on PGA attenuation. Earthq. Spectra 25 (1), 39–69. https://doi.org/10.1193/1.3043904.

Heath, D.C., Wald, D.J., Worden, C.B., Thompson, E.M., Smoczyk, G.M., 2020. A global hybrid Vs30 map with a topographic slope–based default and regional map insets. Earthquake Spectra. https://doi.org/10.1177/8755293020911137, 8755293020911137.

IEA, International Energy Agency, 2020. The Netherlands 2020 energy policy review. IEA Report 258.

Jaarsma, B., Heijnen, N., Veldkamp, H., Schavemaker, Y., 2018. Dinantian carbonates are hot! In *80th EAGE Conference and Exhibition 2018*. European Association of Geoscientists and Engineers, pp. 1–5. https://doi.org/10.3997/2214-4609.201801192 (Vol. 2018, No. 1.

Kooi, H., Landwehr, J.C., Stuurman, R.J., Meerten, J.J.van, Levelt, O., Korff, M., 2021. Indirecte schade van diepe bodemdaling en –stijging bij het Groningen gasveld en gasopslag Norg (Indirect damage due to deep causes of subsidence and uplift at the Groningen gas field and the gas storage Norg). Deltares report 11207096-BGS-0001, 30 August 2021 (in Dutch) 66.

Korswagen, P., Longo, M., Meulman, E., Licciardello, L., Sousamli, M., 2019. Damage Sensitivity of Groningen Masonry – Experimental and Computational Studies (Part 2). NAM Report by Delft University of Technology, p. 512. C31B69WP0-12.

Korswagen, P.A., Longo, M., Rots, J.G., 2022. Fragility curves for light damage of clay masonry walls subjected to seismic vibrations. Bull. Earthq. Eng. 1–35. https://doi.org/10.1007/s10518-022-01404-0.

KNMI, 2022. Earthquakes - complete catalogue for the Netherlands and near surrounding. Royal Netherlands Meteorological Institute Ministry of Infrastructure and Water Manage.

Lee, J., 2019. The social fallout from Pohang's 'Man-Made' Earthquake. The Diplomat. https://thediplomat.com/2019/12/the-social-fallout-from-pohangs-man-made-earthquake/.

Lei, X., Wang, Z., Su, J., 2019. The December 2018 ML 5.7 and January 2019 ML 5.3 earthquakes in South Sichuan basin induced by shale gas hydraulic fracturing. Seismol. Res. Lett. 90 (3), 1099–1110. https://doi.org/10.1785/0220190029.

Majer, E.L., Baria, R., Stark, M., Oates, S., Bommer, J., Smith, B., Asanuma, H., 2007. Induced seismicity associated with enhanced geothermal systems. Geothermics 36 (3), 185–222. https://doi.org/10.1016/j.geothermics.2007.03.003.

Marzocchi, W., Iervolino, I., Giorgio, M., Falcone, G., 2015. When is the probability of a large earthquake too small? Seismol. Res. Lett. 86 (6), 1674–1678. https://doi.org/10.1785/0220150129.

Mijnlieff, H.F., 2020. Introduction to the geothermal play and reservoir geology of the Netherlands. Neth. J. Geosci. 99. https://doi.org/10.1017/njg.2020.2.

Ministry of Economic Affairs and Climate, 2022. Mijnbouwwet, geldend vanaf 5 maart 2022 [Mining law, Last amended on 5 March 2022]. Available on. https://wetten.overheid.nl/BWBR0014168/2022-03-05. Last accessed 4 April, 2022.

Ministry of Economic Affairs and Climate, 2021. Wijziging Mijnbouwbesluit ten behoeve van geothermie [Amendment of the mining decree for geothermal heat and energy], 26 June 2021. Available on. https://www.internetconsultatie.nl/mijnbouwbesluit_aardwarmte. Last accessed 4 April, 2022.

Muntendam-Bos, A.G., De Waal, J.A., 2013. Reassessment of the probability of higher magnitude earthquakes in the Groningen gas field. SodM (State Supervision of Mines) technical report 35.

... and Muntendam-Bos, A.G., Hoedeman, G., Polychronopoulou, K., Draganov, D., Weemstra, C., van der Zee, W., Roest, H., 2022. An overview of induced seismicity in the Netherlands. Neth. J. Geosci. 101. https://doi.org/10.1017/njg.2021.14.

Muntendam-Bos, A.G., Grobbe, N., 2022. Data-driven spatiotemporal assessment of the event-size distribution of the Groningen extraction-induced seismicity catalogue. Sci. Rep. 12, 10119. https://doi.org/10.1038/s41598-022-14451-z.

Nievas, C.I., Bommer, J.J., Crowley, H., Van Elk, J., 2020. Global occurrence and impact of small-to-medium magnitude earthquakes: a statistical analysis. Bull. Earthq. Eng. 18 (1), 1–35. https://doi.org/10.1007/s10518-019-00718-w.

NORSAR, 2018. Review of the public KNMI induced earthquake catalogue from the Groningen gas field. NORSAR Report 157.

Ntinalexis, M., Kruiver, P.P., Ruigrok, E., Rodriguez-Marek, A., Bommer, J.J., Edwards, B., Pinho, R., Spetzler, J., Obando Hernandez, E., Pefkos, M., Bahrampouri, M., van Onselen, E.P., Dost, B., van Elk, J., 2022. A database of ground-motion recordings, site profiles, and amplification factors from the Groningen gas field in the Netherlands. Submitted to Earthquake Spectra.

Olasolo, P., Juárez, M.C., Morales, M.P., Liarte, I.A., 2016. Enhanced geothermal systems (EGS): a review. Renew. Sustain. Energy Rev. 56, 133–144. https://doi.org/10.1016/j.rser.2015.11.031.

Pawley, S., Schultz, R., Playter, T., Corlett, H., Shipman, T., Lyster, S., Hauck, T., 2018. The geological susceptibility of induced earthquakes in the Duvernay play. Geophys. Res. Lett. 45 (4), 1786–1793. https://doi.org/10.1002/2017GL076100.

Richards, J.M., 2015. Social license to operate: hydraulic fracturing-related challenges facing the oil and gas industry. *Oil and Gas*. Nat. Resour. Energy J. 1 (2), 81–163.

Rose, A.N., McKee, J., Urban, M.L., Bright, E.A., Sims, K.M., 2019. *LandScan 2018 High-Resolution Global Population Data Set* (No. LandScan 2018 High-Resolution Global Population Da; 005854MLTPL00). Oak Ridge National Laboratory (ORNL), Oak Ridge, TN (United States).

Ruigrok, E., Dost, B., 2020. Advice on the computation of peak-ground-velocity confidence regions for events in gas fields other than the Groningen gas field. KNMI Technical Report, TR-386 60.

Sarhosis, V., Dais, D., Smyrou, E., Bal, İ.E., 2019. Evaluation of modelling strategies for estimating cumulative damage on Groningen masonry buildings due to recursive induced earthquakes. Bull. Earthq. Eng. 17 (8), 4689–4710. https://doi.org/10.1007/s10518-018-00549-1.

Schmidt, A., Boersma, K., Groenewegen, P., 2018. Management strategies in response to an institutional crisis: the case of earthquakes in the Netherlands. Public Adm. 96 (3), 513–527. https://doi.org/10.1111/padm.12516.

Schoenball, M., Ellsworth, W.L., 2017. A systematic assessment of the spatiotemporal evolution of fault activation through induced seismicity in Oklahoma and southern Kansas. J. Geophys. Res. Solid Earth 122 (12), 10–89. https://doi.org/10.1002/2017JB014850.

Schultz, R., Corlett, H., Haug, K., Kocon, K., MacCormack, K., Stern, V., Shipman, T., 2016. Linking fossil reefs with earthquakes: geologic insight to where induced seismicity occurs in Alberta. Geophys. Res. Lett. 43 (6), 2534–2542. https://doi.org/10.1002/2015GL067514.

Schultz, R., Beroza, G., Ellsworth, W., Baker, J., 2020a. Risk-informed recommendations for managing hydraulic fracturing induced seismicity via traffic light protocols. Bull. Seismol. Soc. Am. https://doi.org/10.1785/0120200016.

Schultz, R., Skoumal, R., Brudzinski, M., Eaton, D., Baptie, B., Ellsworth, W., 2020b. Hydraulic fracturing-induced seismicity. Rev. Geophys. 58 (3), e2019RG000695 https://doi.org/10.1029/2019RG000695.

Schultz, R., Quitoriano, V., Wald, D.J., Beroza, G.C., 2021a. Quantifying nuisance ground motion thresholds for induced earthquakes. Earthquake Spectra. https://doi.org/10.1177/8755293020988025, 8755293020988025.

Schultz, R., Beroza, G., Ellsworth, W., 2021b. A risk-based approach for managing hydraulic fracturing-induced seismicity. Science 372 (6541), 504–507. https://doi.org/10.1126/science.abg5451.

Schultz, R., Beroza, G., Ellsworth, W., 2021c. A strategy for choosing red-light thresholds to manage hydraulic fracturing induced seismicity in North America. J. Geophys. Res.: Solid Earth 126 (12), e2021JB022340. https://doi.org/10.1029/2021JB022340.

Schultz, R., Ellsworth, W.L., Beroza, G.C., 2022. Statistical bounds on how induced seismicity stops. Sci. Rep. 12, 1184. https://doi.org/10.1038/s41598-022-05216-9.

Skoumal, R.J., Brudzinski, M.R., Currie, B.S., 2018. Proximity of Precambrian basement affects the likelihood of induced seismicity in the Appalachian, Illinois, and Williston Basins, central and eastern United States. Geosphere 14 (3), 1365–1379. https://doi.org/10.1130/GES01542.1.

Sintubin, M., 2018. The Groningen case: when science becomes part of the problem, not the solution. Seismol. Res. Lett. 89 (6), 2001–2007. https://doi.org/10.1785/0220180203.

SodM, Staatstoezicht op de Mijnen [State Supervision of Mines], 2014. Risico analyse aardgasbevingen Groningen [Risk assessment gas-earthquakes Groningen (in Dutch)] 19.

Spetzler, J., Evers, L., 2018. Update 2018 Shakemaps for "Maximum considered eartqhauke" scenario in Groningen. Royal Netherlands Meteorological Institute, Ministry of Infrastructure and the Environ. Rep. 44.

Stafford, P.J., Zurek, B.D., Ntinalexis, M., Bommer, J.J., 2019. Extensions to the Groningen ground-motion model for seismic risk calculations: component-to-

component variability and spatial correlation. Bull. Earthquake Eng. 17 (8), 4417–4439. https://doi.org/10.1007/s10518-018-0425-6.
ten Veen, J., de Haan, H., de Bruin, G., Helleman, N., Schöler, W., 2019. Seismic interpretation and depth conversion of the Dinantian carbonates in the Dutch subsurface. Report by SCAN. Netherlands Organization for Applied Scientific Research TNO, p. 100.
ter Heege, J., van Bijsterveldt, L., Wassing, B., Osinga, S., Paap, B., Kraaijpoel, D., 2020. Induced seismicity potential for geothermal projects targeting Dinantian carbonates in the Netherlands. Report by SCAN. Netherlands Organization for Applied Scientific Research TNO, p. 148.
UDG (Ultradiepe Geothermie), 2018. C-217 Green Deal ultradiepe geothermie (UDG). www.greendeals.nl/sites/default/files/downloads/GD217-dealtekst-Ultradiepe-Geothermie.pdf.
van Asselen, S., Erkens, G., Stouthamer, E., Woolderink, H.A., Geeraert, R.E., Hefting, M. M., 2018. The relative contribution of peat compaction and oxidation to subsidence in built-up areas in the Rhine-Meuse delta, The Netherlands. Sci. Total Environ. 636, 177–191. https://doi.org/10.1016/j.scitotenv.2018.04.141.
van Elk, J., Doornhof, D., Bommer, J.J., Bourne, S.J., Oates, S.J., Pinho, R., Crowley, H., 2017. Hazard and risk assessments for induced seismicity in Groningen. Neth. J. Geosci. 96 (5), s259–s269. https://doi.org/10.1017/njg.2017.37.
van Elk, J., Doornhof, D., 2019. Special Report on the Westerwijtwerd Earthquake 22nd May 2019. NAM Report 63.
van der Voort, N., Vanclay, F., 2015. Social impacts of earthquakes caused by gas extraction in the Province of Groningen, The Netherlands. Environ. Impact Assess. Rev. 50, 1–15. https://doi.org/10.1016/j.eiar.2014.08.008.
van Ginkel, J., Ruigrok, E., Stafleu, J., Herber, R., 2022. Development of a seismic site-response zonation map for the Netherlands. Nat. Haz. Earth Syst. Sci. 22 (1), 41–63. https://doi.org/10.5194/nhess-22-41-2022.
van Heekeren, V., Bakema, G., 2015. The Netherlands country update on geothermal energy. Stichting Platform Geothermie, World Geothermal Congress.
van Thienen-Visser, K., Breunese, J.N., 2015. Induced seismicity of the Groningen gas field: History and recent developments. The Leading Edge 34 (6), 664–671. https://doi.org/10.1190/tle34060664.1.
Veldkamp, J., Hegen, D., 2020. Temperature modelling of the Dutch subsurface at the depth of the Dinantian, *Report by SCAN*, Netherlands Organization for Applied Scientific Research TNO 78.
Verdon, J.P., Bommer, J.J., 2020. Green, yellow, red, or out of the blue? An assessment of traffic light schemes to mitigate the impact of hydraulic fracturing-induced seismicity. J. Seismol. https://doi.org/10.1007/s10950-020-09966-9.
Vlek, C., 2019. Rise and reduction of induced earthquakes in the Groningen gas field, 1991–2018: statistical trends, social impacts, and policy change. Environ. Earth Sci. 78 (3), 1–14. https://doi.org/10.1007/s12665-019-8051-4.
Wald, D.J., Quitoriano, V., Worden, C.B., Hopper, M., Dewey, J.W., 2012. USGS "Did You Feel It?" internet-based macroseismic intensity maps. Ann. Geophys. 54 (6) https://doi.org/10.4401/ag-5354.
Zöller, G., Holschneider, M., 2016. The maximum possible and the maximum expected earthquake magnitude for production-induced earthquakes at the gas field in Groningen, The Netherlands. Bull. Seismol. Soc. Am. 106 (6), 2917–2921. https://doi.org/10.1785/0120160220.